



Changing available energy for extratropical cyclones and associated convection in Northern Hemisphere summer

Charles G. Gertler^{a,1} and Paul A. O’Gorman^a

^aDepartment of Earth, Atmospheric and Planetary Sciences, Massachusetts Institute of Technology, Cambridge, MA 02139

Edited by Dennis L. Hartmann, University of Washington, Seattle, WA, and approved January 18, 2019 (received for review July 17, 2018)

The circulation of the Northern Hemisphere extratropical troposphere has changed over recent decades, with marked decreases in extratropical cyclone activity and eddy kinetic energy (EKE) in summer and increases in the fraction of precipitation that is convective in all seasons. Decreasing EKE in summer is partly explained by a weakening meridional temperature gradient, but changes in vertical temperature gradients and increasing moisture also affect the mean available potential energy (MAPE), which is the energetic reservoir from which extratropical cyclones draw. Furthermore, the relation of changes in mean thermal structure and moisture to changes in convection associated with extratropical cyclones is poorly understood. Here we calculate trends in MAPE for the Northern extratropics in summer over the years 1979–2017, and we decompose MAPE into both convective and nonconvective components. Nonconvective MAPE decreased over this period, consistent with decreases in EKE and extratropical cyclone activity, but convective MAPE increased, implying an increase in the energy available to convection. Calculations with idealized atmospheres indicate that nonconvective and convective MAPE both increase with increasing mean surface temperature and decrease with decreasing meridional surface temperature gradient, but convective MAPE is relatively more sensitive to the increase in mean surface temperature. These results connect changes in the atmospheric mean state with changes in both large-scale and convective circulations, and they suggest that extratropical cyclones can weaken even as their associated convection becomes more energetic.

climate change | available energy | extratropical cyclones | convection

Distinct patterns of change have emerged in the thermal structure and moisture content of the Northern Hemisphere extratropical troposphere (1–4), as seen from homogenized radiosonde data (see *Methods*) for the summer season in Fig. 1. Notably, the meridional temperature gradient has weakened in the lower- and middle troposphere (Fig. 1A), and the troposphere has experienced a general moistening (Fig. 1B). The weakening of the meridional temperature gradient is thought to contribute to the observed weakening of eddy kinetic energy (EKE) and cyclone activity levels (5, 6), with implications for regional climate and air quality (7). However, eddy behavior is also affected by changes in moisture content and static stability. For example, amplified low-level warming (Fig. 1A), which is more clearly evident in reanalysis trends that extend to the surface (*SI Appendix, Fig. S1A*), implies decreased static stability in the lower troposphere, which together with increasing specific humidity (Fig. 1B) would tend to increase the growth rates of eddies, opposing the weakening effect from the meridional temperature gradients. Projections of 21st century climate change with coupled climate models also show a decrease in EKE in the Northern Hemisphere in summer that has been linked to weakening lower-tropospheric meridional temperature gradients (8) and increases in extratropical static stability that occurs in the projections in this season (9). The changes in mean thermal structure and moisture could also cause changes in the energy available

to convection; large increases in the convective fraction of precipitation have been observed for all seasons over Eurasia (10), and there is some evidence for increases in convective available potential energy (CAPE) as the climate has warmed (11). However, CAPE is calculated from instantaneous vertical profiles of temperature and humidity and cannot be directly related to changes in mean temperature and moisture in the extratropics.

Mean available potential energy (MAPE) provides a useful framework with which to connect the mean thermal structure (including both meridional temperature gradients and static stability) and moisture content of the extratropical atmosphere to EKE and, as discussed below, to available energy for convection. MAPE is defined as the difference in enthalpy between an atmosphere’s mean state and the minimum-enthalpy state possible from reversible, adiabatic parcel rearrangements (12). MAPE may be calculated neglecting latent heating (dry MAPE) (12) or taking it into account (moist MAPE) (13, 14). EKE scales linearly with dry and moist MAPE in extratropical, baroclinic environments in a wide range of idealized climate model experiments (15–17). A recent study (18) that imposed isolated thermal forcings at different latitudes and levels found that the scaling of EKE with MAPE can break down in some cases, but that it generally performs better than considering the change in meridional temperature gradient or static stability alone. Importantly, EKE also scales linearly with MAPE over the seasonal cycle in the extratropics in both hemispheres based on reanalysis data, and under climate change in coupled model projections, including for intermodel differences (9).

Here, we calculate changes in moist MAPE over recent decades and use the results to better understand observed changes in the circulation. Some recent studies suggest an increasing trend in

Significance

Extratropical cyclones and their associated convection play a central role in the weather of the midlatitudes and are changing with global warming. By analyzing trends in the energy of the mean state of the atmosphere that is available to be converted to kinetic energy, we show how the warming and moistening of the Northern Hemisphere extratropics relates to the observed weakening of extratropical summer cyclones. We also show that the component of this energy that can be released through convection has increased, despite the weakening of extratropical cyclones. Our results provide a unified framework that illustrates how the observed weakening of the extratropical cyclones in summer can occur while at the same time convection becomes more energetic.

Author contributions: C.G.G. and P.A.O. designed research; C.G.G. performed research; C.G.G. analyzed data; and C.G.G. and P.A.O. wrote the paper.

The authors declare no conflict of interest.

This article is a PNAS Direct Submission.

Published under the PNAS license.

¹To whom correspondence should be addressed. Email: cgertler@mit.edu.

This article contains supporting information online at www.pnas.org/lookup/suppl/doi:10.1073/pnas.1812312116/-DCSupplemental.

Published online February 19, 2019.

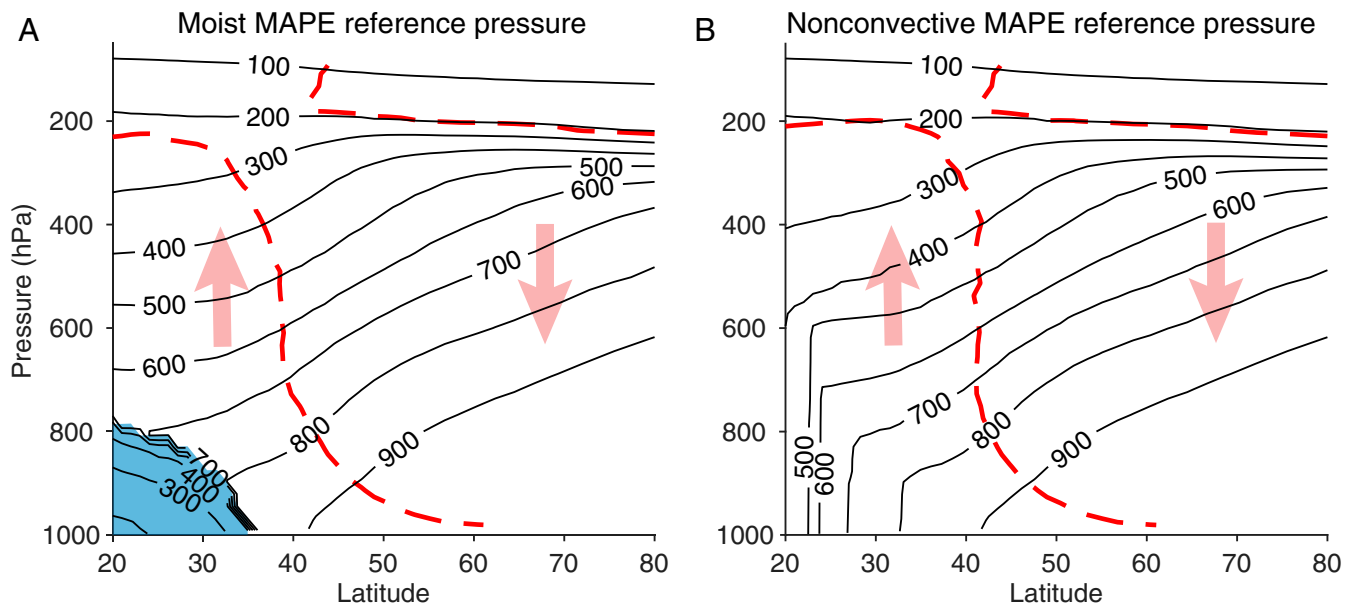


Fig. 2. Visualization of MAPE calculations. Parcel rearrangements in the calculation of (A) moist MAPE and (B) nonconvective MAPE based on climatological JJA zonal-mean temperatures and relative humidities from the ERA-Interim reanalysis (1979–2017). Black contours (contour interval 100 hPa) show the pressure of a given air parcel in the minimum-enthalpy state, referred to as the reference pressure. Arrows schematically indicate vertical motion of parcels. The red dashed lines show where the reference pressure is equal to the pressure. Blue shading in A indicates a region of lower-tropospheric air bounded by a discontinuity in the reference pressure distribution, whose ascent to the upper troposphere corresponds to the release of convective instability.

of the change in EKE. The trends in dry and moist MAPE are also downward and the trend of dry MAPE is similar in magnitude to that of nonconvective MAPE (*SI Appendix, Fig. S5 B and E*).

Interestingly, EKE and nonconvective MAPE are not positively correlated for year-to-year variability when the time series in Fig. 3A are detrended. This different behavior for year-to-year variability compared with longer-term trends is likely because EKE and MAPE have a different relationship for unforced variability compared with forced variability. For forced variability, such as the seasonal cycle of the storm tracks or the response of the storm tracks to climate change, an increase in EKE is associated with an increase in MAPE (9). For unforced variability of the storm tracks, an increase in EKE is associated with amplified heat fluxes which lead to a subsequent decrease in baroclinicity and MAPE (29–31).

In contrast to the decreasing trend in nonconvective MAPE, convective MAPE demonstrates an upward trend of 1.1 J kg^{-1} per decade, with a 90% confidence interval of $[0.7, 1.7] \text{ J kg}^{-1}$ per decade (Fig. 3B). This increase in the energy available to moist convection associated with extratropical cyclones implies a tendency toward more convective precipitation in summer in midlatitudes. Observations show a robust increase in the convective fraction of precipitation over Northern Eurasia (10), and it would be interesting to study changes in the convective fraction of precipitation in other midlatitude regions.

The signs and magnitudes of the trends in nonconvective and convective MAPE and in EKE are similar for narrower (30–70N) and wider (10–90N) latitude bands (*SI Appendix, Fig. S5*). We report the absolute rather than percentage changes in convective MAPE because the absolute changes are less sensitive to the latitude band chosen. Absolute values for all types of MAPE are shown in *SI Appendix, Fig. S6*.

Relation to Surface Temperatures in Idealized Atmospheres

To better understand how climate change can cause changes of opposite sign in nonconvective MAPE and convective MAPE, we next consider how changes in mean surface temperature and meridional surface temperature gradient affect these energetic reservoirs in idealized atmospheres that are representative of Northern Hemisphere summer. We prescribe simple meridional profiles of

surface temperature and vary the mean surface temperature and meridional surface temperature gradient independently. Given that the middle- and lower troposphere are frequently close to neutral to moist convection in summer in the Northern extratropics (32), we construct vertical temperature profiles in idealized atmospheres with prescribed relative humidity such that the virtual temperatures in the troposphere match the virtual temperatures in a reversible moist adiabat of a parcel lifted from the surface (see *Methods* for details). By this construction each individual column in isolation is not conditionally unstable and has no available potential energy, and thus nonzero convective MAPE must arise because of the meridional temperature gradient and the resulting lateral and vertical motion.

Fig. 4 shows the variations in MAPE as a function of mean surface temperature and the mean meridional surface temperature gradient over 20–80N in the idealized atmospheres. The ranges shown are roughly centered on the ERA-Interim mean temperatures and temperature gradients for Northern Hemisphere JJA of 292 K and $0.44 \text{ K degree}^{-1}$. Based on the ERA-Interim trends for JJA, we find that surface temperature increased by roughly 1 K and the surface meridional temperature gradient decreased by roughly $0.02 \text{ K degree}^{-1}$ over the whole period (*SI Appendix, Fig. S7*), and the observed changes in this time period are indicated by the red arrows in Fig. 4. Nonconvective MAPE increases with the meridional temperature gradient as would be expected given that it behaves similarly to dry MAPE, which increases as the meridional temperature gradient squared with some compensation from increases in static stability (33). Nonconvective MAPE also increases with mean surface temperature which likely reflects both increases in latent heating and induced changes in meridional temperature gradients aloft. On the other hand, convective MAPE has two different behavior regimes. For very weak meridional temperature gradients and thus weak large-scale overturning circulation, convective MAPE primarily increases with the meridional temperature gradient because the amount of air that reaches saturation increases with the strength of ascent at lower latitudes. For stronger meridional temperature gradients and thus stronger large-scale overturning, convective MAPE is more strongly a function of mean temperature, and this is the regime in which the observed JJA parameters fall. To understand why convective MAPE is sensitive to mean temperature, we first note that the vertical gradient in

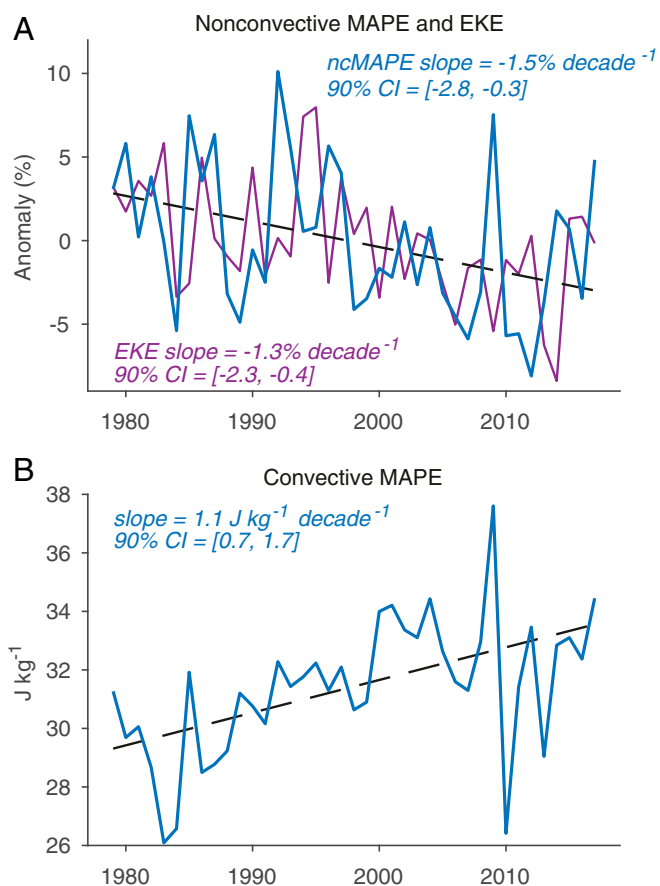


Fig. 3. Time series and trends of energetic reservoirs for summer in the Northern extratropics. (A) Percent anomaly from climatological (1979–2017) mean for nonconvective MAPE (blue line) and EKE (purple line). (B) Convective MAPE, which is defined as the difference between moist MAPE and nonconvective MAPE. All results shown are for JJA over 20–80N based on ERA-Interim reanalysis. Trends and associated 90% confidence intervals are given in each panel. The dashed black lines show the linear best-fit trends for (A) nonconvective MAPE and (B) convective MAPE.

potential temperature along a moist adiabat increases with surface temperature (34), which implies that the ability of a given amount of large-scale ascent to cool the free troposphere and destabilize the column will also increase with temperature. The additional dependence on meridional temperature gradient reflects the ability of stronger temperature gradients to drive more ascent. The idealized atmosphere results show that convective MAPE is relatively more sensitive to mean surface temperature compared with nonconvective MAPE, and this helps explain why convective MAPE can increase in response to mean warming and a weakening meridional temperature gradient even though nonconvective MAPE decreases.

Discussion

Our results show that there have been opposite-signed changes in the energy available to large-scale circulations and associated moist convection in recent decades in Northern extratropical summer, and that these changes are consistent with decreases in EKE and also consistent in sign with observed increases in the convective precipitation fraction. The changes in MAPE thus serve as a bridge between changes in the mean temperature and moisture of the atmosphere and changes in extratropical circulations. The MAPE framework may also be useful for considering past climate states based on surface temperature proxies to the extent that we can assume a vertical stratification in Northern midlatitude summer that is close to moist adiabatic.

While the link between changes in MAPE and EKE has been extensively studied in previous studies (15–18), our results suggest a need for more investigation into connections between the mean state of the extratropical atmosphere (including both mean temperature and temperature gradients) and its convective behavior. For example, future work could compare convective MAPE with other measures of convection, such as instantaneous CAPE and the convective fraction of precipitation, across the seasonal cycle, in idealized simulations, and in warming scenarios. It is also important to investigate the contribution of zonal asymmetries to trends in nonconvective and convective MAPE since these asymmetries are not included in the zonal-mean MAPE considered here.

Decreasing nonconvective MAPE and increasing convective MAPE are consistent with model projections for Northern midlatitude summer over the 21st century (9). However, the large decrease of roughly 6% in nonconvective MAPE found here over recent decades is of similar magnitude to the multimodel-mean projected decrease in nonconvective MAPE over the whole 21st century—a finding consistent with the observed decrease in cyclone activity being near the extreme end of what different climate models simulate for recent decades (6). Substantial components of regional Arctic amplification may result from unforced variability, for example as a result of the Atlantic Multidecadal Oscillation (35) or via teleconnection to tropical Pacific variability (36), and future work could also investigate the contributions of anthropogenic forcing versus unforced variability to trends in MAPE.

Methods

Trends. All trends of time series are calculated using the Theil–Sen estimator, and 90% confidence intervals are calculated using the bootstrapping percentile method. Zonal average trends in temperature and humidity from radiosonde datasets, and reanalysis products subsampled to radiosonde locations, are calculated as follows: stations are binned in 10° latitude bands, and the trend for each pressure level and latitude band is determined as the median trend of the seasonal average at that pressure level among the stations in that latitude band. The use of the median trend in latitude bands limits the influence of outlier trends in the radiosonde data (3).

Temperature and Humidity Data. For the calculation of MAPE, monthly mean temperature and humidity data from 1979 to 2017 with a grid resolution of 2.5° by 2.5° are taken from the ERA-Interim dataset, a global atmospheric reanalysis produced by the European Centre for Medium-Range Weather Forecasts (21). Seasonal-mean temperature and humidity are first calculated at each gridpoint. The zonal mean is then taken for a given year excluding any gridpoints at which the monthly pressure is greater than the monthly surface pressure at that point by more than 25 hPa (the pressure spacing near the surface) for any of the months in the season. The mean surface temperatures and surface meridional temperature gradients shown in *SI Appendix, Fig. S7* are calculated from the zonal and seasonal mean of the 1,000-hPa temperatures at each latitude as calculated above, and then meridionally averaged with area weighting.

Observational temperature data are taken from IUKv2 (3), a radiosonde dataset homogenized by Iterative Universal Kriging to correct for time-varying instrument biases. For direct comparison with IUKv2, ERA-Interim data are subsampled in space and time to the coordinates closest to the station data in the IUKv2 dataset and trends are calculated as described above. We chose ERA-Interim for use in this paper because of its relatively good agreement with the radiosonde data in terms of temperature trends when subsampled to the station locations (compare Fig. 1A with *SI Appendix, Fig. S2A*), whereas other reanalysis products that we analyzed were found to have less good agreement, resulting in MAPE trends different from those presented here, including differences of sign in some cases.

Observational specific humidity data are taken from the homoRS92 dataset, a homogenized global, twice-daily humidity dataset that consists of the dataset described in Dai et al. (4), supplemented with dry-bias corrected data from Vaisala RS92 soundings (37). In reporting relative humidity and specific humidity, this dataset employs a separate homogenized air temperature radiosonde product (38) combined with the homogenized dewpoint depression. Due to missing data in this dataset (which unlike IUKv2 is not iteratively filled), the following processing procedure is applied when determining trends: (i) at individual stations and pressure levels, only days with two measurements are considered, (ii) only months with at least 70% of days are considered, (iii) only JJA averages with all three months present are considered, and (iv) only trends based on at least 70% of years are considered. The zonal-median trend following this

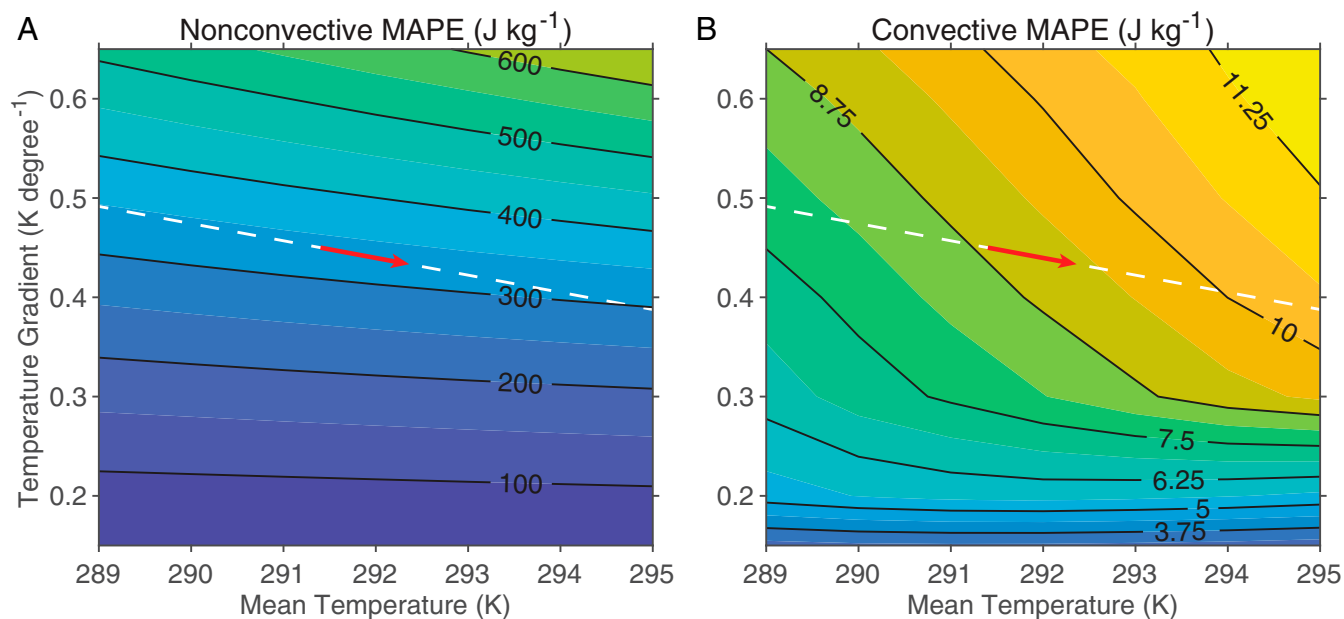


Fig. 4. Energetic reservoirs of idealized atmospheres. (A) Nonconvective MAPE and (B) convective MAPE in idealized atmospheres over the latitude band 20–80°N as a function of mean surface temperature and mean surface meridional temperature gradient in that latitude band. The idealized atmospheres are representative of Northern Hemisphere summer (see *Methods* for details). Contour intervals are 100 J kg⁻¹ in A and 1.25 J kg⁻¹ in B. Red arrows indicate changes in the JJA atmosphere based on ERA-Interim trends over 1979–2017 (see *SI Appendix, Fig. S7* and *Methods* for details), and white dashed line extends these changes along the same slope for clarity.

procedure is shown in Fig. 1B. Trends in ERA-Interim specific humidity data are compared with the observations by subsampling to the homoRS92 dataset station locations. Comparing the radiosonde humidity trends (Fig. 1B) to the subsampled ERA-Interim humidity trends (*SI Appendix, Fig. S3B*) reveals a large discrepancy with much too weak moistening in ERA-Interim. To avoid this bias, we instead use the climatological JJA-mean relative humidity from ERA-Interim (averaged over 1979–2017) as the humidity input to the JJA MAPE calculation for a given year. This approach is consistent with expectations of small trends in relative humidity in the troposphere (39), and it implies trends in specific humidity that are more consistent with the homogenized radiosonde trends in specific humidity (compare Fig. 1B and *SI Appendix, Fig. S2B*). In calculating the JJA specific humidities for *SI Appendix, Fig. S2B* and in our calculations of MAPE, we use the saturation vapor pressure formulae over ice and liquid described in Simmons et al. (40) but with the ice and liquid phases merged using the method described in Wang and Randall (41). The same saturation vapor pressure formulation is also used in calculating the moist adiabats in the idealized atmospheres (see below).

MAPE Calculations. The moist MAPE and its components are calculated for each year using the zonal- and JJA-mean temperatures and relative humidities from ERA-Interim. The temperature for a given year is the JJA-mean temperature for that year. As discussed above, the relative humidity is the climatological (1979–2017) JJA-mean relative humidity. Performing MAPE calculations using time-varying relative humidity (instead of climatological values) from ERA-Interim results in qualitatively similar results (*SI Appendix, Fig. S8*), but the increase in convective MAPE is 0.6 J kg⁻¹ per decade (*SI Appendix, Fig. S8B*), which is roughly half the rate of increase that constant relative humidity implies. The zonal-mean temperatures and relative humidities for each JJA are first interpolated to a 40 × 40 equal-area staggered grid (13) to convert a 2D problem in pressure and latitude coordinates into a 1D problem in pressure coordinates only, although the original latitude for each parcel is stored for use in the calculation of nonconvective MAPE.

To calculate moist MAPE, we use the divide-and-conquer algorithm (14), which is a recursive algorithm that builds a low-enthalpy reference state by dividing the atmospheric domain into smaller subdomains. At each division, the pressure derivative of enthalpy is evaluated at the midpressure of the subdomain and used to order the parcels from top to bottom of the subdomain; the top and bottom halves are then assigned to new subdomains. The divide-and-conquer algorithm has been found to work well in practice (14, 42), and in particular it gives a moist MAPE that is almost identical to that calculated using the exact Munkres algorithm for a similar case to the one considered here (14). We use divide and

conquer rather than Munkres because divide and conquer is faster and more straightforward to adapt to calculate convective and nonconvective MAPE.

To calculate nonconvective MAPE (9), the divide-and-conquer algorithm is modified such that when sorting parcels from top to bottom in a subdomain, parcels from a given initial latitude may not change their vertical ordering (i.e., whether one parcel is above the other). This condition that parcels cannot “leapfrog” in pressure over other parcels from the same initial latitude leads to the continuous remapping of parcel pressure shown in Fig. 2B, in which the reference pressure (the pressure in the minimum-enthalpy state) is a monotonic function of pressure at a given latitude.

To calculate convective MAPE, we simply subtract the nonconvective MAPE from the moist MAPE. The magnitude of convective MAPE is reported per unit mass of the entire atmosphere in the specified latitude band (rather than the mass of a lifted parcel as is the case for CAPE), and as a result the reported values are much smaller than typical CAPE values in convective conditions. For JJA and 20–80N, the mass of the lifted air in the moist MAPE calculation (the blue-shaded region in Fig. 2A) is roughly 6% of the mass of the atmosphere over 20–80N, and the value of convective MAPE of roughly 32 J kg⁻¹ becomes 530 J kg⁻¹ when normalized by the mass of lifted air, which is comparable to typical CAPE values. Convective MAPE should not be confused with generalized CAPE (GCAPE) which is the moist available potential energy of a column of air in isolation (41, 43). The moist available potential energy of the climatological and zonal mean at each latitude in isolation is only nonzero equatorward of 30N, and its meridional average with area weighting over 20–80N is only 1.3 J kg⁻¹ compared with convective MAPE of 32 J kg⁻¹ for the same latitude band. Thus, conditional instability of the mean state does not contribute strongly to convective MAPE.

To calculate dry MAPE, the divide-and-conquer algorithm is used as for the moist MAPE calculation but with the input relative humidity set to zero.

EKE Calculations. To calculate EKE, we first apply a 2.5–6-d Butterworth bandpass filter to four-times-daily horizontal winds on a 2.5° × 2.5° grid from ERA-Interim reanalysis over 1979–2017. Data below the surface pressure are removed (we do not use the approach described above for the monthly temperature and humidity because here we are using instantaneous data). A mass-weighted vertical integral of kinetic energy of the filtered wind time series is calculated at each latitude–longitude grid point to give the local vertically integrated EKE. A JJA- and area-weighted mean of the EKE is then calculated to give the time and spatial mean EKE over the specified latitude band for a given year.

Idealized Atmospheres. Idealized atmospheres are constructed by first imposing profiles of surface air temperature, T_s , as a function of latitude, ϕ :

$$T_s(\phi) = T_{eq} - \Delta_T \sin^2 \phi,$$

where T_{eq} is the surface temperature at the equator and Δ_T is a parameter controlling the meridional surface temperature gradient. Vertical temperature profiles in the atmosphere based on the surface temperatures are then determined as follows. First, reversible moist adiabatic parcel ascents with an assumed initial surface relative humidity of 85% are constructed in which the temperature profile follows a dry adiabat until saturation, after which it follows a saturated moist adiabat. A stratosphere with a constant temperature of 240 K is imposed above the tropopause, with the tropopause defined as the level at which the parcel ascents reach 240 K. While warmer than the real tropopause, this choice limits the extent to which upper-level meridional temperature gradients become much steeper than in the real atmosphere, inflating MAPE values. Next, vertical relative-humidity profiles are imposed with boundary-layer relative humidity of 85% from the surface up to 900 hPa, free-tropospheric relative humidity of 45% between 900 hPa and the tropopause, and stratospheric relative humidity of 0.01%. Using one value of free-tropospheric relative humidity at all latitudes is a simplification, and we chose a value close to the climatological value at lower latitudes where ascending air originates. Lastly, temperature profiles are constructed such that the virtual temperature profile with the imposed relative humidity values matches the virtual temperature profile of the moist adiabat. This procedure allows us to produce a subsaturated atmosphere that is neutral to moist convective instability. As a result, the convective MAPE is driven by the large-scale pattern of ascent and descent rather than having a contribution from conditional instability in the initial condition at a given latitude. In particular, the moist available potential energy of a column of air at a given latitude in isolation, the GCAPE (43), is zero.

We solve for T_{eq} and Δ_T to produce an evenly spaced grid of mean surface temperatures and surface temperature gradients averaged with area

weighting over the latitude band 20–80N. The mean surface temperatures are 289–295 K at increments of 0.5 K, and the mean meridional surface temperature gradients are 0.15–0.65 K degree⁻¹ at increments of 0.05 K degree⁻¹. The moist MAPE and nonconvective and convective components are calculated for each of these idealized atmospheres over 20–80N. The resulting values of moist MAPE and its convective and nonconvective components are shown in Fig. 4.

Based on ERA-Interim over JJA and 20–80N, the mean surface temperature is 292 K and the mean meridional surface temperature gradient is 0.44 K degree⁻¹ (SI Appendix, Fig. S7). At these values, the nonconvective MAPE for the idealized atmosphere is 325 J kg⁻¹ compared with 185 J kg⁻¹ from ERA-Interim, and the convective MAPE for the idealized atmosphere is 9 J kg⁻¹ compared with 32 J kg⁻¹ from ERA-Interim. The larger nonconvective MAPE in the idealized atmosphere likely relates to the meridional temperature gradients aloft being too steep because the idealization of moist-adiabatic lapse rates becomes less accurate at higher latitudes. The smaller convective MAPE in the idealized atmosphere may relate to inaccuracy in the idealized relative-humidity structure since convective MAPE only receives a small contribution from conditional instability of the mean state in ERA-Interim. However, these discrepancies in absolute values are not problematic because our aim in using the idealized atmosphere is to better understand the relative changes in convective and nonconvective MAPE as a function of the surface parameters.

ACKNOWLEDGMENTS. We thank three anonymous reviewers for valuable comments. We are grateful to T. Cronin, H. Wernli, E. Chang, and S. Schemm for helpful discussions; to A. Dai and J. Huang for use of the homoRS92 Dataset; to S. Sherwood for use of the IUK2 dataset; and to the European Center for Medium-Range Weather Forecasts for use of the ERA-Interim reanalysis. C.G.G. acknowledges support from the National Science Foundation Graduate Research Fellowship Program under NSF Grant 1122374. P.A.O. acknowledges support from NSF Grants AGS 1552195 and AGS 1749986.

- Screen JA, Simmonds I (2010) The central role of diminishing sea ice in recent Arctic temperature amplification. *Nature* 464:1334–1337.
- McCarthy MP, Thorne PW, Titchner HA (2009) An analysis of tropospheric humidity trends from radiosondes. *J Clim* 22:5820–5838.
- Sherwood SC, Nishant N (2015) Atmospheric changes through 2012 as shown by iteratively homogenized radiosonde temperature and wind data (IUKv2). *Environ Res Lett* 10:054007.
- Dai A, et al. (2011) A new approach to homogenize daily radiosonde humidity data. *J Clim* 24:965–991.
- Coumou D, Lehmann J, Beckmann J (2015) The weakening summer circulation in the Northern Hemisphere mid-latitudes. *Science* 348:324–327.
- Chang EKM, Ma CG, Zheng C, Yau AMW (2016) Observed and projected decrease in Northern Hemisphere extratropical cyclone activity in summer and its impacts on maximum temperature. *Geophys Res Lett* 43:2200–2208.
- Leibensperger EM, Mickley LJ, Jacob DJ (2008) Sensitivity of US air quality to mid-latitude cyclone frequency and implications of 1980–2006 climate change. *Atmos Chem Phys* 8:7075–7086.
- Harvey BJ, Shaffrey LC, Woollings TJ (2014) Equator-to-pole temperature differences and the extra-tropical storm track responses of the CMIP5 climate models. *Clim Dyn* 43:1171–1182.
- O’Gorman PA (2010) Understanding the varied response of the extratropical storm tracks to climate change. *Proc Natl Acad Sci USA* 107:19176–19180.
- Ye H, Fetzer EJ, Wong S, Lambriksen BH (2017) Rapid decadal convective precipitation increase over Eurasia during the last three decades of the 20th century. *Sci Adv* 3:e1600944.
- Riemann-Campe K, Fraedrich K, Lunkeit F (2009) Global climatology of convective available potential energy (CAPE) and convective inhibition (CIN) in ERA-40 reanalysis. *Atmos Res* 93:534–545.
- Lorenz EN (1955) Available potential energy and the maintenance of the general circulation. *Tellus* 7:157–167.
- Lorenz EN (1979) Numerical evaluation of moist available energy. *Tellus* 31:230–235.
- Stansifer EM, O’Gorman PA, Holt JJ (2017) Accurate computation of moist available potential energy with the Munkres algorithm. *Q J R Meteorol Soc* 143:288–292.
- Schneider T, Walker CC (2008) Scaling laws and regime transitions of macro-turbulence in dry atmospheres. *J Atmos Sci* 65:2153–2173.
- O’Gorman PA, Schneider T (2008) Energy of midlatitude transient eddies in idealized simulations of changed climates. *J Clim* 21:5797–5806.
- O’Gorman PA (2011) The effective static stability experienced by eddies in a moist atmosphere. *J Atmos Sci* 68:75–90.
- Yuval J, Kaspi Y (2017) The effect of vertical baroclinicity concentration on atmospheric macro-turbulence scaling relations. *J Atmos Sci* 74:1651–1667.
- Pan Y, et al. (2017) Earth’s changing global atmospheric energy cycle in response to climate change. *Nat Commun* 8:14367.
- Kim W, Choi Y-S (2017) Long-term change of the atmospheric energy cycles and weather disturbances. *Clim Dyn* 49:3605–3617.
- Dee DP, et al. (2011) The ERA-Interim reanalysis: Configuration and performance of the data assimilation system. *Q J R Meteorol Soc* 137:553–597.
- Madonna E, Wernli H, Joos H, Martius O (2014) Warm conveyor belts in the ERA-Interim dataset (1979–2010). Part I: Climatology and potential vorticity evolution. *J Clim* 27:3–26.
- Rasp S, Selz T, Craig GC (2016) Convective and slantwise trajectory ascent in convection-permitting simulations of midlatitude cyclones. *Mon Weather Rev* 144:3961–3976.
- Pauluis O (2007) Sources and sinks of available potential energy in a moist atmosphere. *J Atmos Sci* 64:2627–2641.
- Seeley JT, Roms DM (2015) Why does tropical convective available potential energy (CAPE) increase with warming? *Geophys Res Lett* 42:10429–10437.
- Singh MS, Kuang Z, Maloney ED, Hannah WM, Wolding BO (2017) Increasing potential for intense tropical and subtropical thunderstorms under global warming. *Proc Natl Acad Sci USA* 114:11657–11662.
- Singh MS, O’Gorman PA (2013) Influence of entrainment on the thermal stratification in simulations of radiative-convective equilibrium. *Geophys Res Lett* 40:4398–4403.
- Agard V, Emanuel K (2017) Clausius-Clapeyron scaling of peak CAPE in continental convective storm environments. *J Atmos Sci* 74:3043–3054.
- Thompson PD (1987) Large-scale dynamic response to differential heating: Statistical equilibrium states and amplitude vacillation. *J Atmos Sci* 44:1237–1248.
- Ambaum MHP, Novak L (2014) A nonlinear oscillator describing storm track variability. *Q J R Meteorol Soc* 140:2680–2684.
- Thompson DWJ, Barnes EA (2014) Periodic variability in the large-scale Southern Hemisphere atmospheric circulation. *Science* 343:641–645.
- Korty RL, Schneider T (2007) A climatology of the tropospheric thermal stratification using saturation potential vorticity. *J Clim* 20:5977–5991.
- Schneider EK (1981) On the amplitudes reached by baroclinically unstable disturbances. *J Atmos Sci* 38:2142–2149.
- Betts AK, Harshvardhan (1987) Thermodynamic constraint on the cloud liquid water feedback in climate models. *J Geophys Res Atmos* 92:8483–8485.
- Chylek P, Folland CK, Lesins G, Dubey MK, Wang MY (2009) Arctic air temperature change amplification and the Atlantic multidecadal oscillation. *Geophys Res Lett* 36:14801.
- Ding Q, et al. (2014) Tropical forcing of the recent rapid Arctic warming in north-eastern Canada and Greenland. *Nature* 509:209–212.
- Wang J, et al. (2013) Radiation dry bias correction of Vaisala RS92 humidity data and its impacts on historical radiosonde data. *J Atmos Ocean Technol* 30:197–214.
- Haimberger L, Tavolato C, Sperka S (2008) Toward elimination of the warm bias in historic radiosonde temperature records—Some new results from a comprehensive intercomparison of upper-air data. *J Clim* 21:4587–4606.
- Sherwood SC, et al. (2010) Relative humidity changes in a warmer climate. *J Geophys Res Atmos* 115:D09104.
- Simmons AJ, Untch A, Jakob C, Källberg P, Undén P (1999) Stratospheric water vapour and tropical tropopause temperatures in ECMWF analyses and multi-year simulations. *Q J R Meteorol Soc* 125:353–386.
- Wang J, Randall DA (1994) The moist available energy of a conditionally unstable atmosphere. Part II. Further analysis of GATE data. *J Atmos Sci* 51:703–710.
- Harris BL, Tailleux R (2018) Assessment of algorithms for computing moist available potential energy. *Q J R Meteorol Soc* 144:1501–1510.
- Randall DA, Wang J (1992) The moist available energy of a conditionally unstable atmosphere. *J Atmos Sci* 49:240–255.